

Pressure-driven transitions in the double perovskite $\text{La}_2\text{CoTiO}_6$: Antiferromagnetic insulator to nonmagnetic metal via antiferromagnetic metal in a double perovskite oxide

Sromona Nandi ¹, Subhadip Pradhan ², Ashis K. Nandy ^{2,*} and Rudra Sekhar Manna ^{1,†}

¹*Department of Physics, Indian Institute of Technology Tirupati, Tirupati, Andhra Pradesh 517619, India*

²*School of Physical Sciences, National Institute of Science Education and Research, An OCC of Homi Bhabha National Institute, Jatni, Odisha 752050, India*



(Received 12 October 2023; revised 27 June 2024; accepted 19 July 2024; published 1 August 2024)

In double perovskite oxides ($A_2BB'O_6$), magnetism often arises from diluted magnetic lattices, created by combining a perovskite structure with localized $3d$ magnetic elements (B) alongside another perovskite lattice containing nearly nonmagnetic delocalized $4d/5d$ elements (B'). Alternatively, the magnetic lattice can consist entirely of $3d$ elements, with one being completely nonmagnetic with a d^0 state. $\text{La}_2\text{CoTiO}_6$ (LCTO), a representative double perovskite oxide, contains Ti in a nonmagnetic state with a d^0 electron configuration due to its 4^+ oxidation state. Experimental evidence shows that LCTO possesses a monoclinic structure (space group $P2_1/n$) and behaves as an antiferromagnet with a Néel temperature of 14.6 K. Through first-principles electronic structure calculations, we uncover that adjusting external hydrostatic pressure induces a sequence of phase transitions: from antiferromagnetic insulator (AFM-I) to antiferromagnetic metal (AFM-M), and ultimately to itinerant nonmagnetic metal (NM-M). The transition from AFM-I to AFM-M at ~ 42 GPa pressure coincides with a shift in spin states, moving from a high-spin (HS) state to a low-spin (LS) state, while Co retains a d^7 configuration. Distortion within the monoclinic structure under pressure plays a pivotal role in the spin-state transition. At the AFM-I to AFM-M transition, we observe a sharp decrease in the ratio of the octahedral volumes occupied by Co and Ti. Such change in ratio is linked to variations in octahedral volumes, akin to a breathing mode distortion. We explore the impact of the breathing mode distortion by examining a highly symmetric theoretical structure (space group $I4/mmm$), achieved by optimizing the structure with all \angle Co-O-Ti angles set to 180° . Remarkably, the LS state in the LCTO theoretical structure persists under ambient pressure conditions, underscoring the unique role of breathing mode distortion in the monoclinic phase, facilitating the HS to LS transition under pressure. In the LS state, LCTO displays metallic behavior, even with a substantial local correlation (Hubbard U) on Co, as large as $U = 6$ eV. The spin-state transition is further elucidated through an energy level diagram, illustrating a significant modification in the crystal field splitting between Co- t_{2g} and Co- e_g levels, driven by the robust hybridization of Co- d and O- p orbitals. Finally, with a further increase in pressure, the system attains the NM-M phase at ~ 130 GPa, leading to the complete suppression of the magnetic moment on Co.

DOI: [10.1103/PhysRevB.110.085101](https://doi.org/10.1103/PhysRevB.110.085101)

I. INTRODUCTION

Double perovskites (DPs) have attracted significant attention in the last few decades due to their unique electronic and magnetic properties owing to the interplay between charge, spin, orbital, and lattice degrees of freedoms [1–4]. This has general chemical formula $A_2BB'O_6$, exhibiting a wide range of compositions due to the natural ability to form perovskite structures in double order which tolerates the altering of multiple transition-metal (TM) cations B and B' of varying sizes and electronic configurations. These TMs are surrounded by oxygen anions forming octahedral units and the A -site cation refers to the various alkaline-/rare-earth elements [5]. Because of their numerous physical phenomena such as half-metallicity, above-room-temperature ferro-/ferrimagnetism,

thermoelectric, magneto-dielectric, magneto-optic, and multiferroic properties, and semiconducting behavior, DPs have received a lot of attention for technological applications, particularly in spintronics [6–10]. Among them, $\text{Sr}_2\text{FeMoO}_6$ [11,12] and $\text{Sr}_2\text{FeReO}_6$ [13,14] are reported as ferrimagnetic (FiM) half-metallic DPs. In contrast to metallic FM DPs, there are antiferromagnetic DPs, e.g., Sr_2FeWO_6 [15], having an insulating ground state can be transformed to FiM metal if one dopes Mo at the W site, i.e., $\text{Sr}_2\text{FeMo}_x\text{W}_{1-x}\text{O}_6$ with $x \geq 0.3$ [16,17]. In addition to that, a list of DPs exhibit Mott insulating behavior due to the delicate balance among spin-orbit coupling (SOC), on-site Coulomb (U) repulsion, and the crystal field effect on the $4d/5d$ TM sites [18–22]. In fact, there are reports of the pressure-induced metal-insulator transition (MIT) for perovskite materials [23–26] which, however, is hardly explored in the case of DPs. The MIT transition is also reported for DPs with partial or full chemical substitution on the A and/or TM sites [27–29]. In addition, there are a few FM/FiM DPs where the spin-state transition is accompanied

*Contact author: aknandy@niser.ac.in

†Contact author: rudra.manna@iittp.ac.in

by a transition from an insulator to nonmagnetic metal via a half-metallic state [30,31] and half-metallic to nonmagnetic metal via a semiconducting state [32]. However, so far, to the best of our knowledge, the MIT in AFM DPs associated with the spin-state transition and, finally, a nonmagnetic metallic state as a function of applied pressure has neither been observed in experiments nor theoretically prescribed.

One interesting class of double perovskite with d^0 electronic configuration at the B' site, e.g., $\text{La}_2\text{CoTiO}_6$ (LCTO), has moderately been studied in experiments [33–35]. This is rather a simple system with Ti in the 4^+ oxidation state suggesting a d^0 electronic configuration. The compound shows an antiferromagnetic ground state with low Néel temperature ($T_N = 14.6$ K). This is due to the fact that the magnetic lattice is formed by the Co atoms only and, hence, it is diluted by the presence of the nonmagnetic Ti atom in LCTO. The nearest-neighbor distance between two Co atoms is roughly $\sqrt{2}$ times as large compared to that in perovskite oxides [36,37]. In general, therefore, relatively weak magnetic exchange coupling between Co magnetic moments is expected. From simple charge balance calculation, Co is expected to show a d^7 electronic configuration due to the Co^{2+} oxidation state. Neutron diffraction reveals the long-range antiferromagnetic order is due to the arrangement of Co spins [34] with a propagation vector ($k = 1/2, 0, 1/2$) [33]. There are some recent studies regarding the cobaltate-titanate oxide heterostructures, hinting about the orbital polarization of Co^{2+} state as a function of electronic correlation and by breaking of electronic symmetry with the formation of a superlattice. Experimentally such a superlattice can be grown as an epitaxial thin film on a substrate [38,39]. Such d -electron configuration (d^7) may result in altering the Co magnetic moment from its high-spin (HS) value to low-spin (LS) value or vice versa due to the change in octahedral geometry. In contrast to the Co^{2+} (d^7) in LCTO, a recent study [40] considering a perovskite, LaCoO_3 with Co^{3+} (d^6), has shown a HS to LS transition associated with the changes in the geometry of CoO_6 octahedra as a function of temperatures.

In this work, within combined experimental and theoretical approaches, we characterize the structural and magnetic behavior of LCTO at ambient pressure. The pressure effects have then been studied within first-principles electronic structure calculations in order to explore the electronic and the associated magnetic properties of LCTO. At ambient pressure, the prepared LCTO has a monoclinic structure with space group $P2_1/n$ as determined from x-ray diffraction (XRD) and shows an antiferromagnetic (AFM) ground state from the Curie-Weiss analysis. The magnetic ground state is consistent with the electronic structure calculations. The insulating nature of having band gap 1.01 eV estimated from the total density of states (DOS) is consistent with the reported resistivity measurement [34]. Such insulating behavior is due to the presence of distortion between the TiO_6 and CoO_6 octahedra as it becomes metallic when the distortion is removed. As we increase pressure, LCTO systematically shows transition from an AFM insulating state to an AFM metallic phase at ~ 42 GPa, and with further increase in pressure, it becomes a nonmagnetic metal at about 130 GPa. In fact, when the system enters this metallic state in the AFM phase, a spin-state transition occurs at that particular pressure and,

hence, the Co moment abruptly jumps from its high-spin state value to the low-spin state value. Such insulator to metal transition associated with the spin-state transition is a rare occurrence in AFMs, and hence, in the case of DP oxides like LCTO, pressure becomes an efficient tool to tailor its physical properties.

The remainder of this paper is written as follows: In Sec. II, we discuss crystal structures and magnetic characterization of the polycrystalline sample in experiment at ambient condition; in Sec. III, the methodology for *ab initio* electronic structure calculations within the density functional theory (DFT) framework is presented; in Sec. IV, we provide the electronic and magnetic properties using fully relaxed atomic coordinates in the unit cell, both for experimental as well as theoretically optimized zero-pressure lattice geometries, and thereafter, we explore the role of breathing modes in CoO_6 and TiO_6 octahedra for the MIT in the high-symmetry theoretical structure; in Sec. V, finally, within first-principles electronic structure calculations we discuss various details of the structural phase transitions along with the associated magnetic and electronic properties as a function of pressure; at the end, Sec. VI summarizes with conclusion of our work on LCTO.

II. EXPERIMENTAL RESULTS AT AMBIENT PRESSURE

A. Crystal structure determination

A polycrystalline sample of LCTO is synthesized by solid-state reaction route and the structural characterization is performed in the powder sample within x-ray diffraction (XRD) at ambient conditions. XRD data are collected using PANalytical Aeris XRD at IIT Tirupati at room temperature, operating $\text{Cu } K_\alpha$ radiation over the angular range $10^\circ \leq 2\theta \leq 90^\circ$ with a 2θ step size of 0.01. Rietveld refinements of the structural parameters were performed using the FULLPROF suite software [41]. The Rietveld refinement on XRD data of LCTO reveals that it crystallizes in a monoclinic structure with space group $P2_1/n$ (No. 14) which is consistent with earlier reports [33,34]. The structure consists of corner-shared oxygen octahedra forming a three-dimensional (3D) network where Co and Ti are at their center surrounded by six oxygens. On the other hand, the La atom is located at the center of the cage formed by the alternating CoO_6 and TiO_6 octahedra along the crystallographic a , b , and c directions; see Fig. 1(a). It is here evident that in the monoclinic phase, the Co-O-Ti chain along the a , b , and c directions deviates significantly from the ideal/undistorted one by changing the angle, $\angle \text{Co-O-Ti}$, from 180° to $\sim 151^\circ$ – 153° . Table I further summarizes all the structural information at room temperature and ambient pressure. The GdFeO_3 -type distortion is also observed in this sample [42]. Due to the larger size of the Co atom compared to the Ti atom, the CoO_6 octahedral volume is expected to be larger than that for the TiO_6 octahedron.

B. Magnetic measurements

The polycrystalline LCTO is used for the magnetization measurements using a magnetic property measurement system (MPMS3, Quantum Design). Figure 1(b) shows the temperature-dependent magnetic susceptibility down to 1.8 K

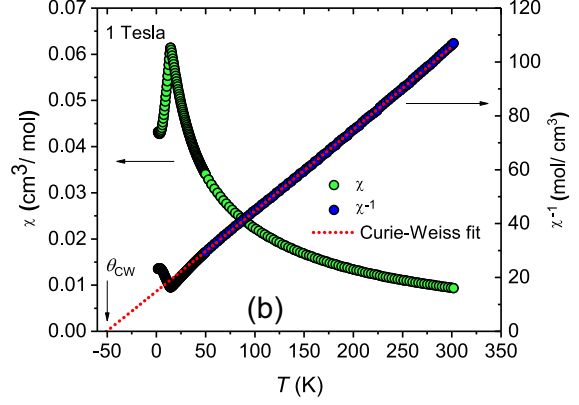
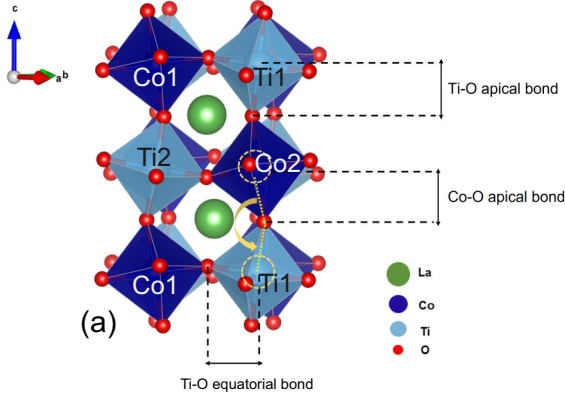


FIG. 1. At ambient pressure: (a) Structure of LCTO with space group $P2_1/n$. The angles \angle Co-O-Ti that connect the TiO_6 and CoO_6 octahedra, both apical and planar, exhibit nearly similar values, approximately 153.2° and 154.3° , respectively. Co and Ti octahedra are distinguished by deep blue and light blue colors, respectively, while La and O atoms are indicated by green and red colors, respectively. (b) The magnetic susceptibility (left axis) and the inverse magnetic susceptibility (right axis) as a function of temperature of LCTO at a magnetic field of $B = 1$ T. The transition temperature T_N is identified as 14.6 K. Utilizing a Curie-Weiss fit, the Curie-Weiss temperature θ_{CW} is determined to be -50.5 K, and the effective magnetic moment is estimated at around $\mu_{\text{eff}} \approx 5.05 \mu_B$ within the experimental unit cell of LCTO.

in an external field of 1 T. As temperature decreases from the room temperature, the magnetization increases in the usual manner obeying the Curie law in the paramagnetic region. However, below 14.6 K the magnetic moment drops significantly showing a peak in the magnetization data. This behavior is not only very typical for an antiferromagnetic (AFM) phase transition, but consistent with the literature [33–35]. Moreover, the Curie-Weiss $\chi = C/(T - \theta_{CW})$ fitting at high temperature between 300 K and 100 K (in the paramagnetic region) yields negative Curie-Weiss temperature, $\theta_{CW} = -50.5$ K, confirming AFM interactions between the spins, and the obtained effective Co moment, μ_{eff} , is $5.05 \mu_B$, and will be compared with the value obtained from the DFT (discussed in the next section). Detailed experimental findings will be published elsewhere.

TABLE I. Table containing structural information (lattice parameters, volumes of the Co and Ti octahedra and the ratio between them, bond lengths and bond angles) of the experimental results obtained from the x-ray diffraction at ambient pressure.

Parameters	Experiment (ambient pressure)
Space group	$P2_1/n$
a (Å)	5.5565
b (Å)	5.5717
c (Å)	7.8566
β (deg)	90.002
V (Å ³)	243.23
$V_{\text{Co-oct}}$ (Å ³)	11.71
$V_{\text{Ti-oct}}$ (Å ³)	10.02
$V_{\text{Co-oct}}/V_{\text{Ti-oct}}$	1.16
$d_{\text{Co-O}}$ (apical) (Å)	2.02
$d_{\text{Ti-O}}$ (apical) (Å)	1.97
$d_{\text{Co-O}}$ (planar) (Å)	2.08
$d_{\text{Ti-O}}$ (planar) (Å)	1.98
\angle Co-O-Ti (apical) (deg)	153.19
\angle Co-O-Ti (planar) (deg)	154.28

III. METHODOLOGY

The electronic and magnetic properties of LCTO without and with pressure have been explored within *ab initio* spin-polarized electronic structure calculations using the projector-augmented wave (PAW) scheme [43,44] in the plane-wave pseudopotential implementation of the DFT code, the Vienna *ab initio* Simulation Package (VASP) [45]. A Perdew-Burke-Ernzerhof (PBE) [46] functional within the generalized gradient approximation (GGA) is adopted for the exchange correlation potential. A k mesh of $8 \times 8 \times 6$ (Γ centered) is used for the momentum-space integration over a full Brillouin zone, while a plane-wave cutoff energy of 500 eV is used for the plane-wave basis expansion in all calculations. In order to consider the electron-electron correlation effect on Co- d electrons, the GGA + U scheme is employed within the Dudarev *et al.* formalism [47]. Here, we have varied the U value between 2 and 6 eV on Co- d (d^7) states while on Ti (d^0), U is always fixed to zero. The internal position coordinates of all atoms have been fully relaxed until the forces are smaller than 10^{-3} eV/Å and the energy convergence cutoff is considered about 10^{-7} eV. In order to determine the optimized zero-pressure structure, we perform the total energy calculations of the unit cell as a function of its volume. This is performed around the experimental unit cell volume via changing the lattice constants uniformly. According to the Birch-Murnaghan (BM) equation [48,49], a fit to the total energy (E) and the unit cell volume (V) is valid around the equilibrium geometry. The details of our BM fitting are given in the Appendix. The total energy (E_0) corresponding to the zero-pressure volume (V_0) point in the BM fitting turns out to be the lowest energy value and the corresponding optimized parameters are further used for the pressure calculations. Achieving true hydrostatic compression requires thorough system relaxation with high precision. Each volume point underwent full geometry optimization until the atomic forces fell below 10^{-3} eV/Å for both FM and AFM magnetic configurations within GGA + U calculations.

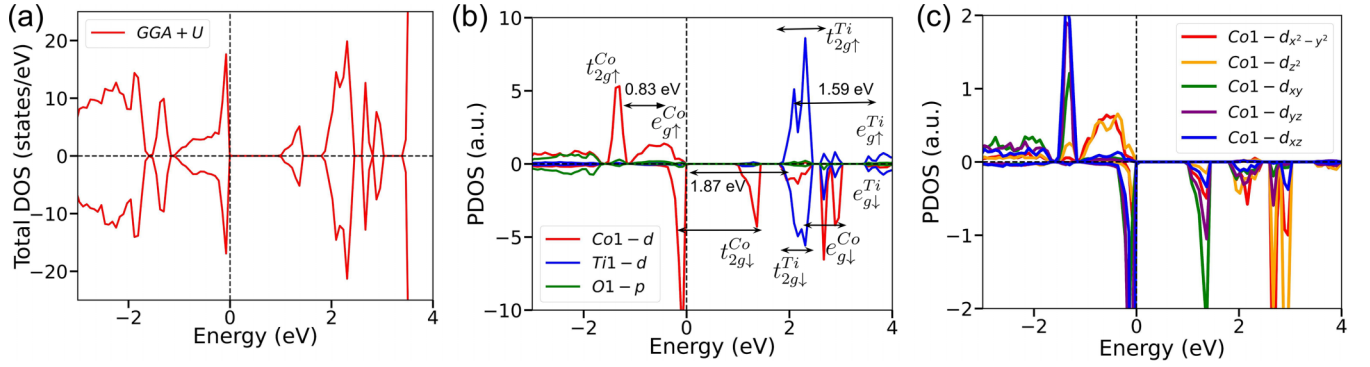


FIG. 2. Electronic structures of LCTO considering AFM state using experimental crystal structure at ambient pressure. The total DOSs in (a) exhibit LCTO as insulator within GGA + U , $U = 2$ eV, calculations. A gap of 1.01 eV is observed in the calculation with a value of U set to 2 eV. In the context of GGA + U calculations, panel (b) depicts the atom-projected partial density of states (PDOS) for the d states of Co1 and Ti1 as well as the O- p state. The octahedral crystal field effect on Co and Ti is responsible for the further designation of d -state orbitals as t_{2g} and e_g . The O- p state is fully occupied, whereas the t_{2g} and e_g orbitals associated with the Ti- d state remain unoccupied. Significantly, the insulating state arises due to the separation of t_{2g}^{Co} states, even when considering GGA (not shown) calculations. For GGA + U calculations, (c) also illustrates the orbital-projected DOS for Co- d orbitals. In all cases, the E_F is set at zero.

Following structure relaxation, a highly accurate static calculation was conducted using the tetrahedron method with Blöchl corrections and an energy convergence criterion of 10^{-7} eV/cell. In order to obtain accurate hydrostatic pressure, the structures were fully relaxed with high accuracy.

IV. DFT RESULTS AT AMBIENT PRESSURE

In order to corroborate with the experimental AFM ground state, in this section, we first discuss the spin-polarized electronic structure results calculated using experimental structure (space group $P2_1/n$) at ambient pressure. The distortion in the experimental structure of LCTO [Fig. 1(a)] is mainly coming from the octahedral tilting measured by the angle $\angle \text{Co-O-Ti}$, given in Table I. The total DOS within the GGA (not shown) calculation reveals insulating AFM behavior with a gap of 0.21 eV. The magnitude of the Co magnetic moment (μ_{Co}) in the AFM configuration is $\sim 2.512 \mu_B$. The addition of correlation, i.e., GGA + U calculation for $U = 2$ eV, gives a slightly enhanced gap value of 1.01 eV [see Fig. 2(a)] which is indeed

in good agreement with the experimental gap value of 1.02 eV [34]. By varying U , we have further compared both FM and AFM configurations defined within the experimental unit cell as well as the high-symmetry undistorted case, presented in Table II. The total energy of the AFM order is always lower than that of the FM state. For $U = 2$ eV, the Co atom carries an absolute magnetic moment μ_{Co} of about $2.6 \mu_B$. The Co^{2+} oxidation state under the HS electronic configuration is offering such magnetic moment. This is in agreement with the expected moment per cobalt of $3 \mu_B$ for the Co^{2+} (d^7) high-spin state in the ordered state. The effective magnetic moment $\sim 5.05 \mu_B$ estimated from the magnetic susceptibility data by fitting the Curie-Weiss law in the paramagnetic region is found to deviate from the spin-only contribution ($3.87 \mu_B$) in our spin-polarized calculations. Such discrepancy is well reported for other materials of having Co^{2+} (d^7) [50–52]. One thus expects that the system may have some unquenched orbital magnetization which contributes to the total magnetic moment. It is however unlikely to have a significantly large orbital moment in 3d oxides. In order to check the effect

TABLE II. The competing magnetic states, AFM and FM, are examined as a function of U (with values of 2, 4, and 6 eV) within GGA+ U calculations for both the theoretically assumed high-symmetry ($I4/mmm$) structure and the experimentally determined low-symmetry ($P2_1/n$) structure. In both scenarios, the AFM state consistently exhibits lower energy (greater stability) compared to the FM state. It should be noted that the stability of the AFM state is examined by considering the most straightforward AFM configuration within a 20-atom unit cell of LCTO. The computed magnetic moment (μ_{Co}) suggests that the LS (HS) state persists within the d^7 electronic configuration of Co for the theoretical structure (the experimental structure) in the electronic configuration of Co. From the gap values in the AFM phase, the last row in the table clearly indicates AFM-M and AFM-I phases for high-symmetry $I4/mmm$ and low-symmetry $P2_1/n$ structures, respectively. The experimentally observed gap is approximately 1.02 eV [34], which corresponds well with the result obtained using $U = 2$ eV.

Parameters	High-symmetric theoretical structure vs low-symmetric experimental structure comparison					
	Undistorted ($I4/mmm$)			Distorted ($P2_1/n$)		
	2 eV	4 eV	6 eV	2 eV	4 eV	6 eV
$E_{\text{FM-AFM}}$ (meV/f.u.)	270	160	150	190	100	100
Moment on Co (μ_{Co} in μ_B)	0.98	0.99	0.99	2.60	2.71	2.80
Gap value (eV)	0	0	0	1.01	1.58	2.08
Magnetic ground state	AFM-M	AFM-M	AFM-M	AFM-I	AFM-I	AFM-I

TABLE III. The detailed structural information of LCTO as function of pressure: lattice parameters, unit cell volumes, $\kappa = \frac{(V_{P \neq 0} - V_{P=0})}{V_{P=0}} \times 100\%$, volumes of the CoO₆ and TiO₆ octahedra, bond lengths and bond angles. Under pressure, κ quantifies the percentage change in volume relative to the optimized volume. The undistorted $I4/mmm$ structure is also optimized in our calculation. The pressure values selected (30, 42, 60, and 130 GPa) in the table result in LCTO entering different states or regimes, e.g., AFM-I, AFM-M, and NM-M in Fig. 4.

Structural parameters	Undistorted	Distorted				
	0 GPa	0 GPa	30 GPa	42 GPa	60 GPa	130 GPa
Space group	$I4/mmm$	$P2_1/n$	$P2_1/n$	$P2_1/n$	$P2_1/n$	$P2_1/n$
a (Å)	5.3722	5.5621	5.2344	5.1683	5.0812	4.8700
b (Å)	5.3722	5.5667	5.3411	5.2736	5.1848	4.9007
c (Å)	7.9659	7.8502	7.4205	7.3254	7.2056	6.9099
β (deg)	90.0	90.3	90.3	90.3	90.3	90.3
V (Å ³)	229.90	243.06	207.65	199.88	189.94	167.24
κ (%)		0	-14.56	-17.76	-21.85	-31.19
$V_{\text{Co-oct}}$ (Å ³)	9.58	11.81	9.39	8.38	7.78	6.69
$V_{\text{Ti-oct}}$ (Å ³)	9.57	10.17	8.98	8.87	8.48	7.38
$V_{\text{Co-oct}}/V_{\text{Ti-oct}}$	1.00	1.16	1.04	0.94	0.92	0.90
$d_{\text{Co-O}}$ (apical) (Å)	2.04	2.06	1.90	1.82	1.79	1.70
$d_{\text{Ti-O}}$ (apical) (Å)	1.94	1.96	1.88	1.88	1.85	1.76
$d_{\text{Co-O}}$ (planar) (Å)	1.87	2.07	1.92	1.86	1.80	1.71
$d_{\text{Ti-O}}$ (planar) (Å)	1.92	1.97	1.89	1.87	1.85	1.77
\angle Co-O-Ti (apical) (deg)	180.00	152.89	156.70	161.79	162.08	169.00
\angle Co-O-Ti (planar) (deg)	180.00	153.51	157.54	162.20	166.32	172.05

of orbital contribution, we have further performed GGA + U calculations with the spin-orbit coupling effect. However, the orbital moment on Co is found to be around 0.17 μ_B along the z direction at ambient pressure. Indeed, it is consistent with the fact that the SOC strength for a $3d$ transition metal (here Co) [39,53] is weak. On the other hand, Ti is found to carry zero magnetic moment, owing to an expected d^0 electronic configuration. These are all evident from the atom-projected Co1- d , Ti- d , and O- p partial density of states (PDOS) presented in Fig. 2(b) for GGA + U calculations. The d -state orbitals of Co and Ti are also marked as t_{2g} and e_g due to the octahedral crystal field effect. Ti- d state is unoccupied whereas the O- p state is fully occupied. These results can be understood by the electronic configuration on the Co1 (Co2) site as $t_{2g\uparrow}^3 e_{g\uparrow}^2 t_{2g\downarrow}^2 (t_{2g\downarrow}^2 e_{g\downarrow}^2 t_{2g\uparrow}^2)$, i.e., a partially filled minority spin channel of Co. Moreover, there is a split between the $t_{2g\downarrow}^{\text{Co}}$ states, even when considering GGA (not shown) calculations, which is responsible for the insulating behavior of this material. Figure 2(c) shows the PDOS of the Co1 sublattice for different d orbitals.

The structure of the LCTO is distorted, i.e., the angle between \angle Co-O-Ti is $\sim 151^\circ$ - 153° , visibly away from the ideal/high-symmetry undistorted structure where the angle between \angle Co-O-Ti is 180° (space group $I4/mmm$). The distortion not only changes the bond angles, but also the bond lengths, given in Table III. As a matter of fact, the local environments as well as the interactions are also changed. We studied the breathing mode [54,55] distortion for the undistorted structure by stretching and squeezing the volume of the Co and Ti octahedra periodically. The volume ratio between the Co and Ti octahedra were changed from 5% to 20% in an equal interval by keeping the unit cell volume fixed. Figure 3(a) shows the structures of LCTO for a few selected (maximum breathing in comparison with the no breathing) breathing parameters, defined as $\delta_B = (1 - V_{\text{Ti}}/V_{\text{Co}})$ where

the structure remains invariant (space group $I4/mmm$). Here we discuss the total DOS and orbital-projected PDOS of Co1 for $\delta_B = +0.33$, $+0.001$, and -0.49 . Figure 3(b) shows the total DOS for all three structures related to $\delta_B = +0.33$, $+0.001$, and -0.49 within GGA + U calculations for $U = 2$ eV. Interestingly, the undistorted structure shows an antiferromagnetic metallic state, indicating distortion plays an important role in tuning the system. The nonzero DOS at E_F confirms that the system is metallic across different δ_B values. Thus, the transition to the metallic state from the insulating state as a function of distortion is accompanied by the electronic phase transition, not driven by the breathing mode distortion, or accompanied by any structural transition. In fact, with the application of hydrostatic pressure, the low-symmetry distorted structure also gives a metallic phase which will be discussed in greater detail in the subsequent section. Figures 3(c), 3(d), and 3(e) show the orbital-projected PDOS for the Co1 sublattice for $\delta_B = +0.33$, $+0.001$, and -0.49 , respectively. For $\delta_B = 0.001$ [see Fig. 3(d)], the d_{yz} and d_{xz} orbitals are almost degenerate; however, the down-spin channels are closer to the Fermi level in comparison to the up-spin channels. A schematic orbital energy level diagram is drawn based on the PDOS, indicating a low-spin state (corresponding magnetic moment on Co 0.98 μ_B), shown in the inset of Fig. 3(d). Thus, the spin-state transition, i.e., from a high-spin state (distorted low-symmetry $P2_1/n$ structure) to a low-spin state (undistorted high-symmetry $I4/mmm$ structure), happens with distortion at ambient pressure. We do not expect any orbital order in this system as the Jahn-Teller effect does not exert significant influence on the octahedral geometries around Co1 and Co2; namely, the octahedral geometries are unchanged. Interestingly, there is a significant change in the PDOS as a function of δ_B ; viz., electronic energy levels shift along the energy axis with varying δ_B . As a matter of fact,

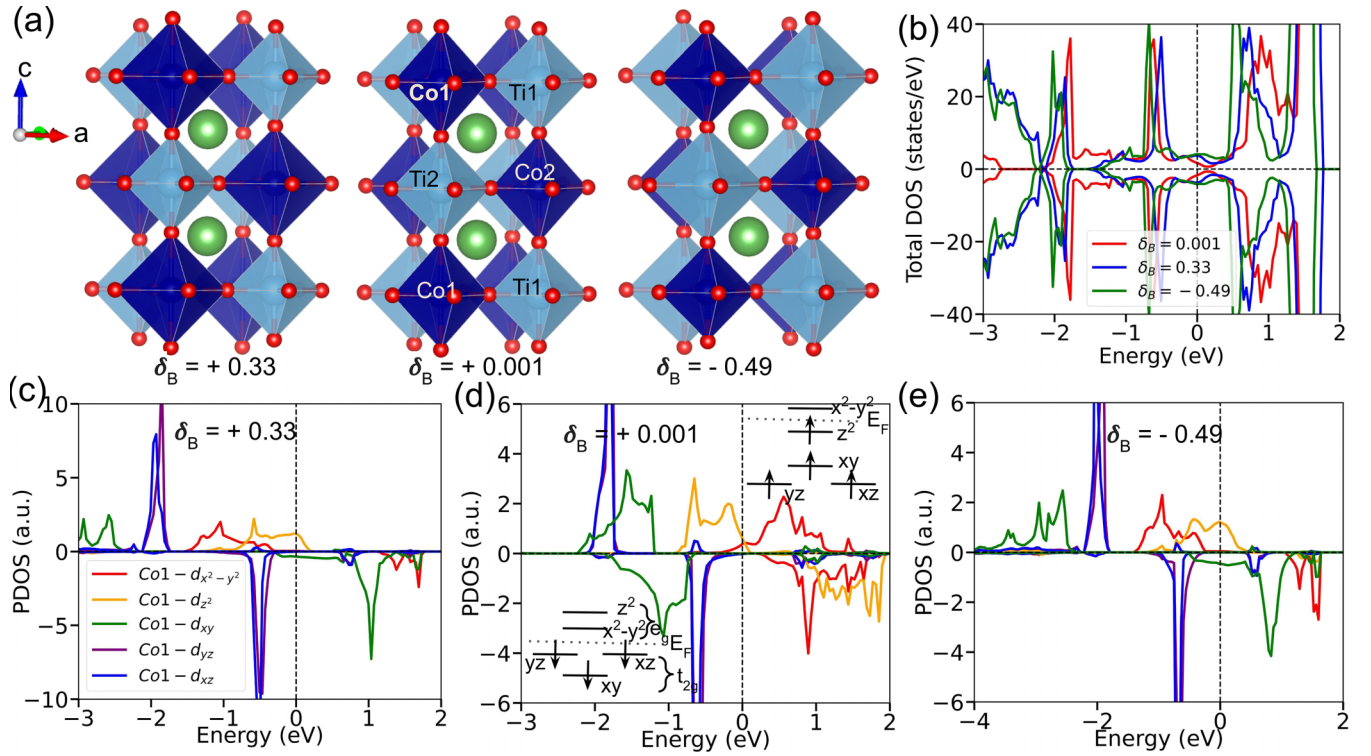


FIG. 3. The impact of a breathing-type distortion on the octahedra of TiO_6 and CoO_6 . In this context, we adopt the high-symmetry $I4/mmm$ structure, leading to an assumed angle of $\angle \text{Co-O-Ti} = 180^\circ$. Keeping unit cell volume fixed, the alteration in the volume of the TiO_6 and CoO_6 octahedra is quantified by introducing the parameter δ_B , defined as $\delta_B = (1 - V_{\text{Ti}}/V_{\text{Co}})$. (a) The configurations displaying the octahedral network of CoO_6 (deep blue) and TiO_6 (light blue) in LCTO are illustrated for values of $\delta_B = +0.33$, $+0.001$, and -0.49 . Ti and Co atoms are situated at the center of the octahedra while La and O atoms are marked in green and red colors, respectively. Changing the δ_B value under the $I4/mmm$ phase does not introduce a gap at E_F , as clearly evident from the total DOS shown in (b). However, the orbital-projected DOS considering Co1 in panels (c)–(e) exhibits distinct changes in orbital characteristics as a function of δ_B ; for instance, electronic energy levels shift along the energy axis with varying δ_B . We have performed our calculations within GGA + U for $U = 2$ eV. Remarkably, the d^7 electronic configuration of Co remains unchanged despite the presence of the breathing distortion. At $\delta_B = 0.001$, the magnetic moment on Co is determined to be $0.98 \mu_B$, supporting a LS state; see the energy level diagram presented in the inset of (d). Within the metallic phase, a significant disparity in octahedral volume ($\delta_B = +0.33$ and -0.49) triggers a transition to the HS state, resulting in an increase in the magnetic moment of Co to $0.9 \mu_B$ and $2.45 \mu_B$, respectively. Importantly, throughout all examined cases, the Ti electronic configuration remains consistent at the d^0 state. The coordinate system in an octahedron is defined such that the position of oxygen atoms align along the x , y , and z axes locally, establishing a well-defined reference for orbitals. In that scenario, the t_{2g} manifold comprises d_{xy} , d_{yz} , and d_{xz} orbitals, while the e_g manifold comprises $d_{x^2-y^2}$ and d_{z^2} orbitals.

the change in the ratios of the octahedral volume induces a high-spin state for $\delta_B = -0.49$ (corresponding magnetic moment in Co $2.45 \mu_B$) in comparison to the low-spin state for $\delta_B = +0.33$ (corresponding magnetic moment in Co $0.9 \mu_B$). Importantly, throughout all examined cases, the Ti electronic configuration remains consistent at the d^0 state. Thus, the breathing mode also plays an important role in transforming the spin-state transition in this material while the structure ($I4/mmm$) remains unchanged.

The minimum energies obtained for both AFM and FM Co-spin configurations at ambient pressure for both undistorted (theoretically high-symmetry $I4/mmm$) and distorted (experimentally low-symmetry $P2_1/n$) structures within GGA + U calculations for U values of 2, 4, and 6 eV. Table II consolidates the energy difference between the configurations, magnetic moments, gap values, and the corresponding magnetic ground states as a function of U values. For both the structures, AFM remains the ground state providing the lower energy in comparison to FM configuration. The es-

timated magnetic moment (μ_{Co}) reveals that the theoretical high-symmetry $I4/mmm$ structure shows a low-spin (LS) state with $\mu_{\text{Co}} = 0.98\text{--}0.99 \mu_B$ whereas the experimental low-symmetry $P2_1/n$ structure remains in the high-spin (HS) state with $\mu_{\text{Co}} = 2.6\text{--}2.8 \mu_B$. The ground state as a function of U remains at the AFM metallic state for the undistorted $I4/mmm$ structure whereas it is insulating for the distorted $P2_1/n$ structure. In fact, the experimentally obtained gap value 1.02 eV [34] corresponds to the gap value obtained for $U = 2$ eV. As a matter of fact, studies under pressure were carried out for $U = 2$ eV.

There is a structural transition when the distortion is removed; namely, the undistorted tetragonal $I4/mmm$ structure is modified to a distorted cubic $P2_1/n$ structure. However, there is no structural change in the distorted structure when the pressure was applied and the system transforms to a metallic state from an insulating state, which will be discussed in the subsequent section. There is some similarity with the nickelate systems where the metal to insulator transition is

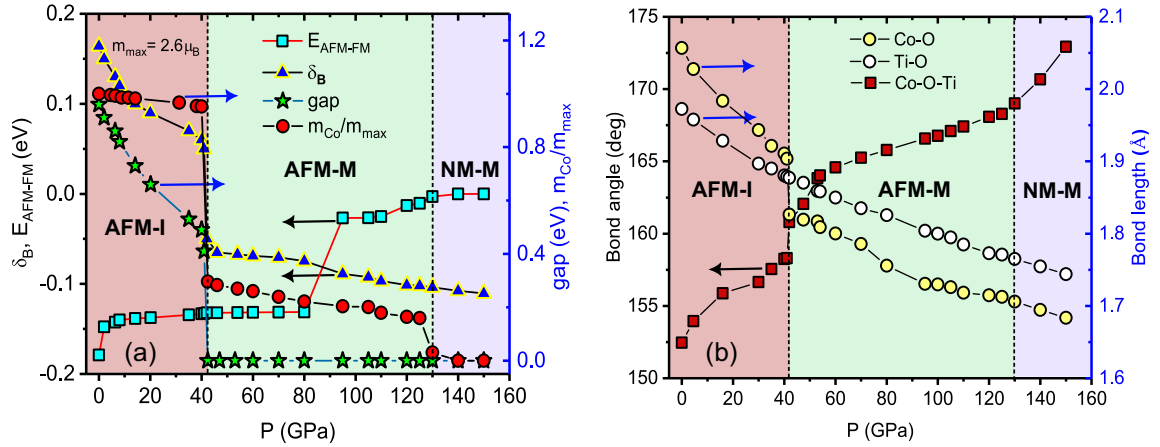


FIG. 4. Pressure-induced variations in various quantities provide support for the existence of various stable phases: AFM insulator (AFM-I), AFM metal (AFM-M), and nonmagnetic metal (NM-M). Three well-defined phases are evident in different colors (light red, light green, and light violet) with their boundary lines clearly depicted as shown in panel (a). The magnetic moment of Co (red circles), expressed in units of m_{max} , experiences a sudden decrease coinciding with a sharp change in δ_B (blue triangle) around 42 GPa pressure. This transition is accompanied by the gap closing (green star), signifying a transition from an insulator to a metal in the AFM phase. The AFM phase consistently maintains lower energy until the second transition to the NM-M phase occurs around a pressure of 130 GPa, as indicated by the cyan square. Remarkably, a transition from a HS to a LS state in the magnetic moment of Co becomes apparent under pressure, ultimately vanishing in the NM-M phase. In panel (b), we illustrate the pressure-dependent structural changes, specifically along the c axis (apical), including variations in Co-O and Ti-O bond lengths (yellow and white circles, respectively), as well as \angle Co-O-Ti (red square). The simulations are carried out with a U value of 2 eV.

accompanied by a structural change [55,56]. However, the undistorted breathing mode structure, i.e., the breathing mode in addition to the $GdFeO_3$ -type distortion, cannot open a gap at the Fermi level with large U values, cf. Table II, in contrast to the nickelate systems. Nevertheless, AFM still remains the ground state of the system.

V. DFT RESULTS AT VARYING PRESSURE

A. Structural changes under hydrostatic pressure

In this section, we discuss the hydrostatic pressure studies, with an applied maximum of 150 GPa on the distorted low-symmetry structure ($P2_1/n$). We tune the system from an antiferromagnetic insulating (AFM-I) state to a nonmagnetic metallic (NM-M) state via an antiferromagnetic metallic (AFM-M) state by the application of hydrostatic pressure. Note that the AFM-M state can also be achieved from the AFM-I state as a function of distortion, discussed in Sec. IV. Table III summarizes all the theoretical optimized structural information, i.e., lattice parameters, unit cell volumes, volumes of the Co and Ti octahedra, percentage change in volume defined as $\kappa = \frac{(V_{P \neq 0} - V_{P=0})}{V_{P=0}} \times 100\%$, the ratio between the octahedra volumes, bond lengths (Co-O and Ti-O for both apical and equatorial), and bond angles (\angle Co-O-Ti for both apical and equatorial) used for the calculations. This includes the optimized high-symmetry ($I4/mmm$) undistorted structure at ambient pressure and low-symmetry distorted ($P2_1/n$) structure at ambient pressure, as well as a few selected pressure points (30, 42, 60, and 130 GPa) corresponding to the various regimes, i.e., AFM-I, AFM-M, and NM-M, of the phase diagram. Under pressure, the monoclinic space group $P2_1/n$ remains the same with more distorted structure in terms of changes in bond lengths and angles.

Figure 4 shows a detailed phase diagram containing all the phases, i.e., AFM-I, AFM-M, and NM-M, as a function of hydrostatic pressure. At ambient pressure, the system is an AFM-I with a band gap of around 1.01 eV at the Fermi level. As pressure increases the band gap decreases almost linearly followed by a sudden jump at around 42 GPa when the system enters into an AFM-M state by closing the band gap, shown in Fig. 4(a). In fact, a number of parameters have been estimated and plotted in the same graph showing significant changes across this phase boundary. The pressure-dependent Co moment normalized to its maximum value ($2.6 \mu_B$) decreases linearly till 42 GPa followed by a dramatic change upon entering the AFM-M state. The moment decreases further, and at around 130 GPa, the moment abruptly becomes vanishingly small, indicating that the system transforms to a NM-M state. The breathing parameter (δ_B) also shows an abrupt jump at the AFM-I to AFM-M phase transition. Interestingly, the jump happens when the volume of the Co and Ti octahedra are almost equal. As the minimum energy for both the AFM and FM configurations is rather small, we calculated the energy difference between the configurations as a function of pressure and plotted in the same graph. Throughout, the AFM phase maintains the lower energy. In fact, there is a slight increase in the energy difference till 130 GPa; then it becomes zero drastically which is consistent with the fact that the system enters to the NM-M state.

Two other parameters, namely, the bond lengths and the bond angles, also show interesting consequences when the system enters to this metallic state. Figure 4(b) shows the pressure variation of the Co-O and Ti-O apical (c -axis) bond lengths and \angle Co-O-Ti apical bond angle. Other bond lengths (equatorial bond lengths) and \angle Co-O-Ti equatorial bond angle show (not plotted here for clarity) similar behavior. With the increase of the applied pressure, the Ti-O bond lengths

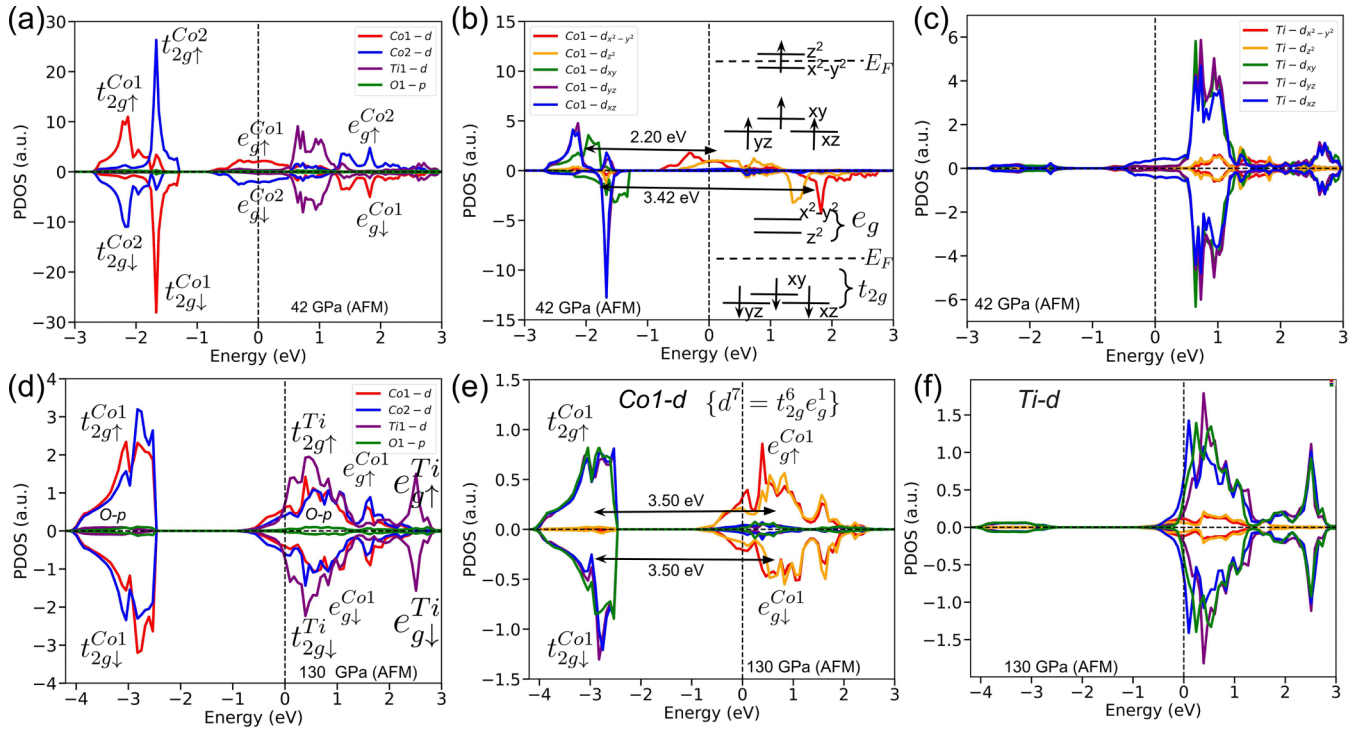


FIG. 5. In the AFM-M phase corresponding to the pressure $P = 42$ GPa, the following features in the PDOS profile are illustrated: (a) atom-projected PDOS of Co1- d , Co2- d , Ti- d , and O- p ; (b) orbital-projected PDOS for Co1; (c) orbital-projected PDOS for Ti. The level diagram depicted in the inset of (b), which outlines the orbital nature of the Co- d state, illustrates the LS state of the d^7 electronic configuration. Ti remains at the d^0 state. The development of the magnetic moment within the LS state of Co is linked to the exchange splitting within the e_g level. Nonetheless, this exchange splitting gradually diminishes to zero as pressure continues to rise, typically around 130 GPa. The atom-projected PDOS is presented in (d) for Co1- d , Co2- d , Ti- d , and O- p , while the orbital-projected PDOSs for Co1- d and Ti- d are depicted in (e) and (f), respectively. An almost NM-M phase becomes evident at 130 GPa pressure from the calculations, even though a nearly negligible Co moment is observed in our calculations. These calculations are performed within GGA + U for $U = 2$ eV.

gradually decrease, while the Co-O bond lengths and the \angle Co-O-Ti angle undergo significant abrupt changes at the AFM-I to AFM-M phase transition. In fact, under the application of hydrostatic pressure in a p -band oxide Rb_4O_6 , the spin-state transitions [i.e., a transition from a high-spin (HS) state to a low-spin (LS) state and, ultimately, to a nonmagnetic state is characterized by the total quenching of the magnetic moment] can develop various magnetic and electronic phases concomitantly: AFM insulator, FM insulator, FM half-metal, and finally, nonmagnetic (NM) metal [57]. Interestingly, in such oxides the magnetism is driven by the p -electron-based anionogenic magnetic order where one observes partially filled π bands associated with the O_2 molecular orbital energy levels [58–60].

Note that all the calculations, on the basis of which the phase diagrams are constructed (Fig. 4), were done for $U = 2$ eV. As electron correlation U plays a vital role for the metal-insulator transition, we also calculated (not shown) the pressure variation of the band gap for different U values. The gap values increase with the increase of the U values and the system takes higher pressure to get into the metallic phase as expected. However, the onset of the antiferromagnetic metallic state is robust for all the U values studied.

At very high pressure (~ 140 GPa), we tested the structural stability of LCTO through phonon calculations (not shown here) and identified an imaginary optical mode at the Γ

point. This mode corresponds primarily to oxygen displacement, indicating a pressure-induced ferroelectric-like lattice instability [61]. Detailed analysis of pressure-driven ferroelectricity requires extensive study, which could open new avenues for future research in LCTO under pressure.

B. Spin-state transition under pressure and associated electronic structures

As illustrated in Fig. 4, the system exhibits distinct magnetic behaviors under different pressure conditions. To be more specific, the system progresses from an AFM-I phase to an AFM-M phase at $P \approx 42$ GPa and subsequently, at $P \approx 130$ GPa, it undergoes a further transition, entering a NM-M phase. The initial transition from the AFM-I (as shown in Fig. 2) to the AFM-M phase is associated with a spin-state transition, during which the Co magnetic moment undergoes a sudden change from its HS state value to the LS state value. Therefore, we provide a comprehensive examination by analyzing the electronic structures computed for different atoms at two critical pressure values, 42 GPa and 130 GPa. In Fig. 5(a), the atom-projected PDOS is particularly depicting the contributions from the Co1- d , Co2- d , Ti- d , and O- p states at 42 GPa. Around E_F , the Co atoms, specifically their d orbital, contribute almost entirely compared to the other atoms. Due to the antiferromagnetic alignment of the

Co spins in LCTO, the spin-polarized d -orbital contribution from the Co1 sublattice is exactly opposite to that arising from the Co2 sublattice. As a result, in the AFM-M phase (42 GPa pressure), LCTO exhibits a typical metallic behavior in the total DOS, characterized by the existence of nonzero DOS at E_F . Figures 5(b) and 5(c) present the corresponding orbital-projected PDOS of Co1- d and Ti- d states. As shown in Fig. 5(c), it is clear that Ti is in a nonmagnetic state, as its d -orbital PDOS features are situated above E_F . The electronic configuration of the Ti atom remains as expected d^0 configuration, confirming its 4^+ oxidation state. However, the magnetic moment on Co undergoes an abrupt decrease, reaching a value of approximately $0.97 \mu_B$. From Fig. 5(b), it is crucial to emphasize that the number of d electrons on Co remains unchanged to d^7 , which in turn leads to a transition in its spin-state due to the applied pressure of about 42 GPa. The corresponding energy level diagram presented in the inset illustrates a LS state for Co1 (Co2) having the electronic configuration as $t_{2g}^3 e_g^2 t_{2g}^1 e_g^1$ ($t_{2g}^3 t_{2g}^3 e_g^1$). Prior to this transition, Co has a magnetic moment of approximately $2.6 \mu_B$ at pressures below 42 GPa, indicating a HS state with an electronic configuration of $t_{2g}^3 e_g^2 t_{2g}^1$; see also Fig. 2(b). The reordering of energy levels is correlated with the sudden decrease in the δ_B value at around 42 GPa pressure, as depicted in Fig. 4(a). Additionally, as pressure is applied, the Ti-O bond lengths gradually decrease, while the Co-O bond lengths and the \angle Co-O-Ti angle undergo significant abrupt changes, as depicted in Fig. 4(b). These changes profoundly affect the electronic structure of LCTO, particularly the energy level gap between t_{2g} and e_g orbitals on Co. In this context, t_{2g} and e_g levels are ascribed to Co d based on the splitting occurring within the CoO_6 octahedral geometry. In the up-spin channel, the energy separation between the t_{2g} and e_g orbitals is initially approximately 0.83 eV under ambient conditions [Fig. 2(b)] but increases to around 2.2 eV at the pressure corresponding to the transition from AFM-I to AFM-M [Fig. 5(b)]. A similar trend is also observed in the down-spin channel. We observe that this results in a crossover of energy levels, with the $e_{g\uparrow}$ level being positioned above the $t_{2g\downarrow}$ level. This, in turn, effectively reduces the exchange splitting within the t_{2g} bands, enabling the emergence of a t_{2g}^6 electronic configuration at 42 GPa pressure. Another significant change is observed in the bandwidth of both t_{2g} and e_g levels. The observed bandwidth increase correlates with reduced Co-O bond lengths in the CoO_6 octahedra under pressure, enhancing Co- d and O- p state hybridization. However, at ambient condition (HS state), the unequal Co-O (apical) and Co-O (planar) bond lengths within CoO_6 octahedra lead to additional splitting of the t_{2g} and e_g levels in the down-spin channel, as seen in the orbital-projected PDOS of cobalt in Fig. 5(b). The gap value at E_F within GGA is approximately 0.21 eV, while within GGA + U [see total DOS Fig. 2(a)], it is approximately 1.01 eV, consistent with its insulating nature. Before transitioning to the LS state with a sudden band gap closure at E_F , there is a gradual decrease in the band gap while the system remains in the HS state. In the LS state, where the Co- t_{2g} level is fully occupied, the extra electron eventually populates the e_g level of Co partially, thereby causing the system to exhibit metallic properties. Therefore, the expected magnetic moment on Co is $1 \mu_B$ and the calculated moment of $0.97 \mu_B$ provides strong

evidence of the transition to the LS state. In the pressure range approximately from 42 GPa to 130 GPa, LCTO maintains its AFM-M phase with the magnetic moment of Co showing minimal variation; see Fig. 4(a). Note that the energy levels linked to the LS state bear a striking resemblance to the configuration observed in the theoretically optimized undistorted high-symmetry ($I4/mmm$) structure under ambient pressure conditions; see Fig. 3(d).

Once the pressure exceeds 130 GPa, the exchange splitting becomes zero, leading to the complete suppression of the Co moment. This leads to another transition of the AFM-M phase into an NM-M phase at a critical pressure of 130 GPa. Furthermore, the phase diagram shown in Fig. 4(a) clearly demonstrates that the energy values for the considered AFM and FM configurations are degenerate. In both cases, the computed Co moment is found to be zero. Figure 5(d) presents the atom-projected PDOS for the Co1- d , Co2- d , Ti- d , and O- p states, while Figs. 5(e) and 5(f) depict the corresponding orbital-projected PDOS for the Co1- d and Ti- d states, respectively. Under such high-pressure conditions, it is expected that the hybridization between Co- d and O- p states will be significantly enhanced owing to the further reduction in bond lengths. Comparing Figs. 5(a) and 5(d), a significant expansion in the bandwidths of the t_{2g} and e_g levels can be noted. The Co- t_{2g} orbitals are observed to be pushed even lower with respect to E_F , potentially leading to a more significant reduction in the effective exchange splitting. Indeed, as demonstrated in the PDOS calculations shown in Fig. 5(e), the exchange splitting in the Co- t_{2g} /Co- e_g level has substantially diminished, approaching zero. Hence, the magnetic moment on Co is entirely quenched, while the partial occupancy in the e_g band keeps the metallic characteristics in LCTO. The increased bandwidth under pressure can counterbalance the impact of correlation effects (U), rendering the absence of a magnetic moment on Co even for a large value of U . In other words, the NM-M phase remains stable even with an increase in U up to 6 eV. The results presented here are derived from GGA + U calculations with a U value of 2 eV.

Typically, applied pressure leads to reduced interatomic distances, causing a decrease in the previously defined breathing parameter, δ_B . As pressure in LCTO increases, the Co- t_{2g} energy level in Figs. 2(b), 5(a), 5(b) 5(d), and 5(e) experiences a discernible shift, as depicted by its position relative to E_F . The reduction in CoO_6 octahedral volume primarily modifies the octahedral crystal field splitting and simultaneously enhances d - p hybridization due to shorter Co-O bond lengths, resulting in increased bandwidth of t_{2g} and e_g orbitals. In Fig. 6, we summarize the pressure-dependent studies within an energy level diagram, which illustrates a microscopic mechanism for the spin-state transition. Here, the ultimate energy level diagrams (presented on the right and left sides for HS and LS states, respectively) are illustrated, considering the hybridization between nonmagnetic O- p and Co- d orbitals in the presence of exchange splitting Δ_{EX} . Furthermore, the final energy levels are designated based on the combined impact of the crystal field and hybridization, with Δ_{CF} representing the resulting separation between t_{2g} and e_g levels. The critical aspect of the transition from HS to LS is the energy level crossing between e_g^\uparrow and t_{2g}^\downarrow , primarily occurring due to the renormalization in hybridization under

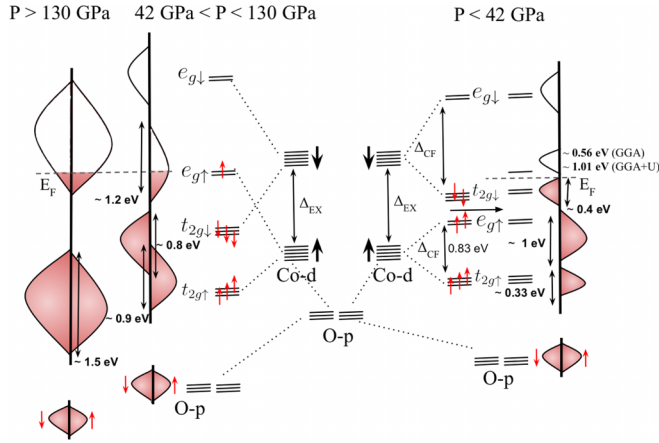


FIG. 6. The energy level diagram of Co- d orbitals offers insight into the mechanism underpinning the pressure-induced spin-state transition in LCTO, in accordance with the findings from DFT analysis. The energy levels of Co- t_{2g} and Co- e_g orbitals in both the up- and down-spin channels are displayed on the right side (HS state), demonstrating the impact of hybridization between Co- d and O- p orbitals within an octahedral arrangement. At the far right, we provide schematics of the Co PDOS as computed at ambient pressure. On the left side, the energy levels are adjusted to account for changes in hybridization occurring within a pressure range of 42 to 130 GPa, ultimately resulting in the manifestation of a LS state. Beyond 130 GPa, the magnetic moment of cobalt (Co) is entirely quenched. The Co PDOSs for 42 and 130 GPa pressures are schematically shown at the far left.

pressure. As an illustrative example, the bandwidth of t_{2g}^\uparrow increases nearly threefold, going from around 0.33 eV under ambient conditions to approximately 0.9 eV at 42 GPa; see the schematics of Co PDOS in Fig. 6. The abrupt decrease in δ_B at about 42 GPa pressure (see Fig. 4) signifies that concurrent with the crossover, a metallic behavior in LCTO appears with the E_F lying in the e_g^\uparrow state. The e_g^\uparrow state exhibits a notably wide bandwidth of approximately 1.6 eV, indicating the robustness of the metallic state even when we increase the electron correlation parameter U to 6 eV. At the AFM-M to NM-M transition point (130 GPa pressure), the t_{2g} level is pushed even further below E_F , with a Δ_{CF} of approximately 3.50 eV, as illustrated in Fig. 5(e). The bandwidth, which is also approximately 1.5 eV, is a consequence of even stronger hybridization effects. In this situation, our calculations reveal complete quenching of the exchange splitting in the t_{2g} and e_g levels, maintaining the electronic configuration as $t_{2g}^6 e_g^1$ (LS state), but resulting in a zero magnetic moment on the Co site. The mechanism depicted in Fig. 6 hence demonstrates how changes in pressure significantly impact the energy levels and bandwidths of Co- t_{2g} and Co- e_g orbitals, leading to a series of transitions: from AFM-I to AFM-M, and ultimately to NM-M. In addition, we have estimated the Hund's coupling (J) and crystal field splitting (Δ) values from the PDOSs in three different pressure regions: 30 GPa (AFM-I), 42 GPa (AFM-M), and 130 GPa (NM-M), tabulated in Table IV. This estimation is carried out by analyzing roughly the center of bands, t_{2g} and e_g in the PDOS. The separation, $E(t_{2g}^{\text{Co}\uparrow}) - E(e_g^{\text{Co}\uparrow})$, for two different spin channels provides an approximate estimation of

TABLE IV. The variation of Hund's coupling J and crystal field splitting Δ in three different regions, namely, at 8 GPa (AFM-I), 42 GPa (AFM-M), 130 GPa (NM-M).

P (GPa)	Estimated J value (eV)	Estimated Δ value (eV)
8	1.16	0.83
42	0.6	2.2
130	0.0	3.5

J , while the separation, $E(t_{2g}^{\text{Co}\uparrow}) - E(e_g^{\text{Co}\uparrow})$, within the same spin channel offers an estimate of the crystal field splitting Δ [62–64]. The values as a function of pressure exhibit a systematic variation, clarifying the spin state transition in LCTO. In the future, we would like to do a very detailed study on this aspect by performing model calculations.

VI. SUMMARY AND CONCLUSIONS

The double perovskite oxide $\text{La}_2\text{CoTiO}_6$ was first examined experimentally through synthesis and magnetic measurements, followed by a detailed investigation using first-principles electronic structure calculations within density functional theory. This comprehensive study aimed to understand the magnetic and transport properties of $\text{La}_2\text{CoTiO}_6$ under different external pressure conditions. At ambient pressure, the structure is monoclinic with space group $P2_1/n$ and it shows an insulating behavior with antiferromagnetic ground state below $T_N = 14.6$ K at ambient pressure. However, with the application of hydrostatic pressure on the experimental structure, studied within first-principles electronic structure calculations, we can tune the magnetic and transport properties, viz., antiferromagnetic insulator to antiferromagnetic metal at around 42 GPa, and finally to itinerant nonmagnetic metal at around 130 GPa. Interestingly, antiferromagnetic insulator to antiferromagnetic metal transition is accompanied with a spin-state transition (high-spin to low-spin state) while Co and Ti remain in the d^7 and d^0 electronic configuration, respectively. The spin-state transition under pressure is found to be robust with U up to 6 eV. The structural distortion, particularly a breathing mode distortion near the critical pressure point, facilitates the spin-state transition as the system transitions into the metallic phase. Furthermore, we observe a low-spin state even under ambient pressure conditions in a theoretically high-symmetry structure where the lattice distortions in the monoclinic structure are removed. The introduction of breathing mode by changing the ratio of the Co and Ti octahedra governs an increase in Co magnetic moment in the metallic phase. The PDOS and the corresponding energy level diagram illustrate that the pressure-induced spin-state transition is a result of both the octahedral crystal field splitting in Co- d orbitals (splitting to t_{2g} and e_g levels) and the bandwidths, mainly driven by the strong hybridization between Co- d and O- p orbitals. The nonmagnetic metallic phase at high pressure (above 130 GPa) is characterized by the total quenching of the Co magnetic moment. Thus, $\text{La}_2\text{CoTiO}_6$ is a rare antiferromagnetic double perovskite oxide where the insulator to metal transition can be tuned as a function of hydrostatic pressure/distortion/even changing

the breathing parameter which is accompanied by a spin-state transition. In the future, experimental validation of these phase transitions can be conducted by subjecting the synthesized material to hydrostatic pressure conditions.

ACKNOWLEDGMENTS

R.S.M. acknowledges financial support from SERB for his Early Career Research Award (File No. ECR/2018/000999/PMS). The authors would like to acknowledge IIT Tirupati for providing experimental setup for the sample preparation and the high-performance computing (HPC) cluster for DFT calculations, and IIT Mandi for the magnetization measurements. In addition, HPC support from IISER Tirupati is also acknowledged. A.K.N. and S.P. acknowledge support from the National Institute of Science Education and Research (NISER), Department of Atomic Energy, Government of India, for funding the research work through Project No. RIN-4001. A.K.N. and S.P. acknowledge the computational resources, the Kalinga cluster, at NISER, Bhubaneswar, India. A.K.N. thanks Prof. P. M. Oppeneer for the Swedish National Infrastructure for Computing (SNIC) facility and VASP simulations.

APPENDIX: BIRCH-MURNAGHAN FITTING

As pressure increases, the unit cell volume decreases, leading to a reduction in the bond lengths between atoms. The total energy obtained from self-consistent calculations for specific volumes was fitted to the Birch-Murnaghan (BM) isothermal equation of state [48,49], as shown here,

$$E(V) = E_0 + \frac{9V_0B_0}{16} \left[\left(\frac{V_0}{V} \right)^{\frac{2}{3}} - 1 \right]^3 B'_0 + \left[\left(\frac{V_0}{V} \right)^{\frac{2}{3}} - 1 \right]^2 \left[6 - 4 \left(\frac{V_0}{V} \right)^{\frac{2}{3}} \right], \quad (\text{A1})$$

where B and B'_0 are the bulk modulus and its pressure derivative, respectively, and E_0 is the total energy at the equilibrium volume V_0 [65–67].

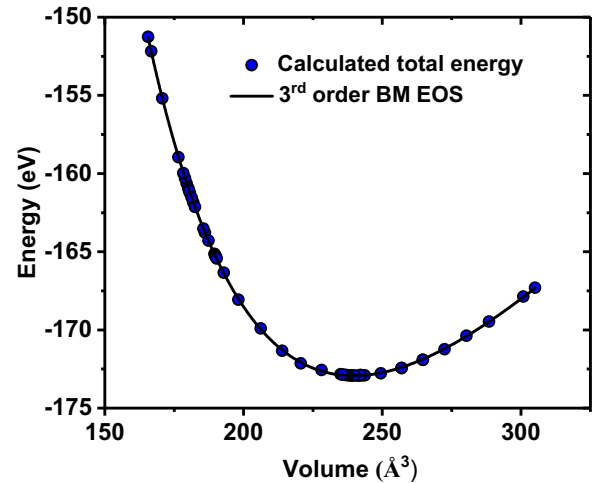


FIG. 7. The *ab initio* calculated energy (E) versus volume (V) data of $\text{La}_2\text{CoTiO}_6$ within GGA + U calculation considering $U = 2$ eV. This is fitted to the Birch-Murnaghan equation.

By fitting the *ab initio* computed energy value as a function of volume, the calculated parameters are as follows: $E_0 = -172.92$ eV, $V_0 = 239.87$ Å³, $B_0 = 142.78$ GPa, and $B'_0 = 4.42$.

To determine the pressure, the derived fitting parameters were then incorporated into the pressure-volume BM relation [48,49] as

$$P(V) = \frac{3B_0}{2} \left[\left(\frac{V_0}{V} \right)^{7/3} - \left(\frac{V_0}{V} \right)^{5/3} \right] \times \left\{ 1 + \frac{3}{4}(B'_0 - 4) \left[\left(\frac{V_0}{V} \right)^{2/3} - 1 \right] \right\}. \quad (\text{A2})$$

We have performed these calculations within GGA + U for $U = 2$ eV where the structure remains unaffected with space group $P2_1/n$.

The ambient pressure lattice parameters for $\text{La}_2\text{CoTiO}_6$, which represent the ground state parameters, are determined through the BM fitting shown in Fig. 7. The smallest volume point on the plot corresponds to the $\text{La}_2\text{CoTiO}_6$ structure at zero pressure, and volumes less than this corresponds to the structure under pressure.

-
- [1] D. I. Khomskii and G. A. Sawatzky, Interplay between spin, charge and orbital degrees of freedom in magnetic oxides, *Solid State Commun.* **102**, 87 (1997).
- [2] Y. Murakami, H. Kawada, H. Kawata, M. Tanaka, T. Arima, Y. Moritomo, and Y. Tokura, Direct observation of charge and orbital ordering in $\text{La}_{0.5}\text{Sr}_{1.5}\text{MnO}_4$, *Phys. Rev. Lett.* **80**, 1932 (1998).
- [3] E. Dagotto and Y. Tokura, Strongly correlated electronic materials: Present and future, *MRS Bull.* **33**, 1037 (2008).
- [4] A. Pal, K. Anand, N. Patel, A. Das, S. Ghosh, P. T.-W. Yen, S.-M. Huang, R. K. Singh, H. D. Yang, A. K. Ghosh, and S. Chatterjee, Interplay of spin, phonon, and lattice degrees in a hole-doped double perovskite: Observation of spin-phonon coupling and magnetostriction effect, *J. Appl. Phys.* **132**, 223906 (2022).
- [5] R. H. Mitchell, *Perovskite: Modern and Ancient* (Almay Press, Ontario, Canada, 2002).
- [6] M. N. Iliev, P. Padhan, and A. Gupta, Temperature-dependent Raman study of multiferroic $\text{Bi}_2\text{NiMnO}_6$ thin films, *Phys. Rev. B* **77**, 172303 (2008).
- [7] T. Nakagawa, Magnetic and electrical properties of ordered perovskite $\text{Sr}_2(\text{FeMo})\text{O}_6$ and its related compounds, *J. Phys. Soc. Jpn.* **24**, 806 (1968).
- [8] M. Fiebig, T. Lottermoser, D. Frohlich, A. V. Goltsev, and R. V. Pisarev, Observation of coupled magnetic and electric domains, *Nature (London)* **419**, 818 (2002).

- [9] K.-I. Kobayashi, T. Kimura, H. Sawada, K. Terakura, and Y. Tokura, Room-temperature magnetoresistance in an oxide material with an ordered double-perovskite structure, *Nature (London)* **395**, 677 (1998).
- [10] K. I. Kobayashi, T. Kimura, Y. Tomioka, H. Sawada, K. Terakura, and Y. Tokura, Intergain tunneling magnetoresistance in polycrystals of the ordered double perovskite $\text{Sr}_2\text{FeReO}_6$, *Phys. Rev. B* **59**, 11159 (1999).
- [11] D. D. Sarma, P. Mahadevan, T. Saha-Dasgupta, S. Ray, and A. Kumar, Electronic structure of $\text{Sr}_2\text{FeMoO}_6$, *Phys. Rev. Lett.* **85**, 2549 (2000).
- [12] D. D. Sarma, A new class of magnetic materials: $\text{Sr}_2\text{FeMoO}_6$ and related compounds, *Curr. Opin. Solid State Mater. Sci.* **5**, 261 (2001).
- [13] S. K. Pandey, A. K. Nandy, P. Kumari, and P. Mahadevan, Microscopic origin of room-temperature ferromagnetism in the double perovskite $\text{Sr}_2\text{FeReO}_6$, *Phys. Rev. B* **105**, 214422 (2022).
- [14] J. Longo and R. Ward, Magnetic compounds of hexavalent rhenium with the perovskite-type structure, *J. Am. Chem. Soc.* **83**, 2816 (1961).
- [15] H. Kawanaka, I. Hase, S. Toyama, and Y. Nishihara, Electronic state of Fe in double perovskite oxide Sr_2FeWO_6 , *J. Phys. Soc. Jpn.* **68**, 2890 (1999).
- [16] T. Nakagawa, K. Yoshikawa, and S. Nomura, Electrical properties and Mössbauer effect in the system $\text{Sr}_2(\text{FeMo}_x\text{W}_{1-x})\text{O}_6$, *J. Phys. Soc. Jpn.* **27**, 880 (1969).
- [17] S. Ray, A. Kumar, S. Majumdar, E. V. Sampathkumaran, and D. D. Sarma, Transport and magnetic properties of $\text{Sr}_2\text{FeMo}_x\text{W}_{1-x}\text{O}_6$, *J. Phys.: Condens. Matter* **13**, 607 (2001).
- [18] H. L. Feng, S. Calder, M. P. Ghimire, Y.-H. Yuan, Y. Shirako, Y. Tsujimoto, Y. Matsushita, Z. Hu, C.-Y. Kuo, L. H. Tjeng, T.-W. Pi, Y.-L. Soo, J. He, M. Tanaka, Y. Katsuya, M. Richter, and K. Yamaura, $\text{Ba}_2\text{NiOsO}_6$: A Dirac-Mott insulator with ferromagnetism near 100 K, *Phys. Rev. B* **94**, 235158 (2016).
- [19] A. S. Cavichini, M. T. Orlando, J. B. Depianti, J. L. Passamai, Jr., F. Damay, F. Porcher, and E. Granado, Exotic magnetism and spin-orbit-assisted Mott insulating state in a $3d$ - $5d$ double perovskite, *Phys. Rev. B* **97**, 054431 (2018).
- [20] M. P. Ghimire, L.-H. Wu, and X. Hu, Possible half-metallic antiferromagnetism in an iridium double-perovskite material, *Phys. Rev. B* **93**, 134421 (2016).
- [21] H. Chen, Magnetically driven orbital-selective insulator-metal transition in double perovskite oxides, *npj Quantum Mater.* **3**, 57 (2018).
- [22] N. Narayanan, D. Mikhailova, A. Senyshyn, D. M. Trots, R. Laskowski, P. Blaha, K. Schwarz, H. Fuess, and H. Ehrenberg, Temperature and composition dependence of crystal structures and magnetic and electronic properties of the double perovskites $\text{La}_{2-x}\text{Sr}_x\text{CoIrO}_6$ ($0 \leq x \leq 2$), *Phys. Rev. B* **82**, 024403 (2010).
- [23] M. Q. Cai, G. W. Yang, X. Tan, Y. L. Cao, L. L. Wang, W. Y. Hu, and Y. G. Wang, First-principles study of pressure-induced metal-insulator transition in BiNiO_3 , *Appl. Phys. Lett.* **91**, 101901 (2007).
- [24] R. Qiu, E. Bousquet, and A. Cano, Pressure-induced insulator-metal transition in EuMnO_3 , *J. Phys.: Condens. Matter* **29**, 305801 (2017).
- [25] M. C. Bennett, G. Hu, G. Wang, O. Heinonen, P. R. C. Kent, J. T. Krogel, and P. Ganesh, Origin of metal-insulator transitions in correlated perovskite metals, *Phys. Rev. Res.* **4**, L022005 (2022).
- [26] J.-G. Cheng, J.-S. Zhou, J. B. Goodenough, J. A. Alonso, and M. J. Martínez-Lope, Pressure dependence of metal-insulator transition in perovskites RNiO_3 ($R = \text{Eu, Y, Lu}$), *Phys. Rev. B* **82**, 085107 (2010).
- [27] A. Poddar and S. Das, Metal-insulator transition in double perovskite $\text{Sr}_2\text{Fe}(\text{Re, W})\text{O}_6$ compound, *Phys. B: Condens. Matter* **344**, 325 (2004).
- [28] S. Nazir, Insulator-to-half metal transition and enhancement of structural distortions in $\text{Lu}_2\text{NiIrO}_6$ double perovskite oxide via hole-doping, *Sci. Rep.* **11**, 1240 (2021).
- [29] Y. Krockenberger, K. Mogare, M. Reehuis, M. Tovar, M. Jansen, G. Vaitheeswaran, V. Kanchana, F. Bultmark, A. Delin, F. Wilhelm, A. Rogalev, A. Winkler, and L. Alff, $\text{Sr}_2\text{CrOsO}_6$: End point of a spin-polarized metal-insulator transition by $5d$ band filling, *Phys. Rev. B* **75**, 020404(R) (2007).
- [30] S. Lv, X. Liu, H. Li, L. Han, Z. Wang, and J. Meng, Insulator-metal transition driven by pressure and B-site disorder in double perovskite $\text{La}_2\text{CoMnO}_6$, *J. Comput. Chem.* **33**, 1433 (2012).
- [31] H. J. Zhao, H. Zhou, X. M. Chen, and L. Bellaiche, Predicted pressure-induced spin and electronic transition in double perovskite $R_2\text{CoMnO}_6$ ($R = \text{rare-earth ion}$), *J. Phys.: Condens. Matter* **27**, 226001 (2015).
- [32] Y. Qian, H. Wu, R. Lu, W. Tan, C. Xiao, and K. Deng, Effect of high-pressure on the electronic and magnetic properties in double perovskite oxide $\text{Sr}_2\text{FeMoO}_6$, *J. Appl. Phys.* **112**, 103712 (2012).
- [33] E. Rodríguez, M. L. López, J. Campo, M. L. Veiga, and C. Pico, Crystal and magnetic structure of the perovskites La_2MTiO_6 ($M = \text{Co, Ni}$), *J. Mater. Chem.* **12**, 2798 (2002).
- [34] K. L. Holman, Q. Huang, T. Klimczuk, K. Trzebiatowski, J. W. G. Bos, E. Morosan, J. W. Lynn, and R. J. Cava, Synthesis and properties of the double perovskites La_2NiVO_6 , La_2CoVO_6 , and $\text{La}_2\text{CoTiO}_6$, *J. Solid State Chem.* **180**, 75 (2007).
- [35] M. Yuste, J. C. Perez-Flores, J. R. de Paz, M. T. Azcondo, F. García-Alvarado, and U. Amador, New perovskite materials of the $\text{La}_{2-x}\text{Sr}_x\text{CoTiO}_6$ series, *Dalton Trans.* **40**, 7908 (2011).
- [36] S. Middey, A. K. Nandy, S. K. Pandey, P. Mahadevan, and D. D. Sarma, Route to high Néel temperatures in $4d$ and $5d$ transition metal oxides, *Phys. Rev. B* **86**, 104406 (2012).
- [37] H. K. Chandra, K. Gupta, A. K. Nandy, and P. Mahadevan, Ferroelectric distortions in doped ferroelectrics: $\text{BaTiO}_3:M$ ($M = \text{V-Fe}$), *Phys. Rev. B* **87**, 214110 (2013).
- [38] S. Lee, A. T. Lee, A. B. Georgescu, G. Fabbri, M.-G. Han, Y. Zhu, J. W. Freeland, A. S. Disa, Y. Jia, M. P. M. Dean, F. J. Walker, S. Ismail-Beigi, and C. H. Ahn, Strong orbital polarization in a cobaltate-titanate oxide heterostructure, *Phys. Rev. Lett.* **123**, 117201 (2019).
- [39] A. T. Lee, H. Park, and S. Ismail-Beigi, Origin of the orbital polarization of Co^{2+} in $\text{La}_2\text{CoTiO}_6$ and $(\text{LaCoO}_3)_1 + (\text{LaTiO}_3)_1$: A DFT+ U and DFMT study, *Phys. Rev. B* **103**, 125105 (2021).
- [40] D. Takegami, A. Tanaka, S. Agrestini, Z. Hu, J. Weinen, M. Rotter, C. Schüßler-Langeheine, T. Willers, T. C. Koethe, T. Lorenz, Y. F. Liao, K. D. Tsuei, H.-J. Lin, C. T. Chen, and L. H. Tjeng, Electronic structure evolution across the Peierls metal-insulator transition in a correlated ferromagnet, *Phys. Rev. X* **13**, 011037 (2023).

- [41] J. Rodríguez-Carvajal, Recent advances in magnetic structure determination by neutron powder diffraction, *Phys. B: Condens. Matter* **192**, 55 (1993).
- [42] M. O’Keeffe and B. G. Hyde, Some structures topologically related to cubic perovskite ($E2_1$), ReO_3 ($D0_9$) and Cu_3Au ($L1_2$), *Acta Crystallogr. B: Struct. Sci.* **33**, 3802 (1977).
- [43] P. E. Blöchl, Projector augmented-wave method, *Phys. Rev. B* **50**, 17953 (1994).
- [44] G. Kresse and D. Joubert, From ultrasoft pseudopotentials to the projector augmented-wave method, *Phys. Rev. B* **59**, 1758 (1999).
- [45] G. Kresse and J. Furthmüller, Efficient iterative schemes for *ab initio* total-energy calculations using a plane-wave basis set, *Phys. Rev. B* **54**, 11169 (1996).
- [46] J. P. Perdew, K. Burke, and M. Ernzerhof, Generalized gradient approximation made simple, *Phys. Rev. Lett.* **77**, 3865 (1996).
- [47] S. L. Dudarev, G. A. Botton, S. Y. Savrasov, C. J. Humphreys, and A. P. Sutton, Electron-energy-loss spectra and the structural stability of nickel oxide: An LSDA+U study, *Phys. Rev. B* **57**, 1505 (1998).
- [48] F. Birch, Finite elastic strain of cubic crystals, *Phys. Rev.* **71**, 809 (1947).
- [49] F. D. Murnaghan, Finite deformations of an elastic solid, *Am. J. Math.* **59**, 235 (1937).
- [50] H.-J. Koo, R. K. Kremer, and M.-H. Whangbo, Orbital magnetic moments of the high-spin Co^{2+} ions at axially-elongated octahedral sites: Unquenched as reported from experiment or quenched as predicted by theory? *Inorg. Chem.* **59**, 18319 (2020).
- [51] M. C. Viola, M. J. Martinez-Lope, J. A. Alonso, J. L. Martinez, J. M. De Paoli, S. Pagola, J. C. Pedregosa, M. T. Fernandez-Diaz, and R. E. Carbonio, Structure and magnetic properties of Sr_2CoWO_6 : An ordered double perovskite containing Co^{2+} (HS) with unquenched orbital magnetic moment, *Chem. Mater.* **15**, 1655 (2003).
- [52] S. Lee, M.-C. Lee, Y. Ishikawa, P. Miao, S. Torii, C. Won, K. Lee, N. Hur, D.-Y. Cho, and T. Kamiyama, Crystal and magnetic structures of $\text{La}_2\text{CoPtO}_6$ double perovskite, *ACS Omega* **3**, 11624 (2018).
- [53] R. A. Cowley, W. J. L. Buyers, C. Stock, Z. Yamani, C. Frost, J. W. Taylor, and D. Prabhakaran, Neutron scattering investigation of the d - d excitations below the Mott gap of CoO , *Phys. Rev. B* **88**, 205117 (2013).
- [54] P. V. Balachandran and J. M. Rondinelli, Interplay of octahedral rotations and breathing distortions in charge-ordering perovskite oxides, *Phys. Rev. B* **88**, 054101 (2013).
- [55] A. Hampel and C. Ederer, Interplay between breathing mode distortion and magnetic order in rare-earth nickelates RNiO_3 within DFT + U , *Phys. Rev. B* **96**, 165130 (2017).
- [56] S. Johnston, A. Mukherjee, I. Elfimov, M. Berciu, and G. A. Sawatzky, Charge disproportionation without charge transfer in the rare-earth-element nickelates as a possible mechanism for the metal-insulator transition, *Phys. Rev. Lett.* **112**, 106404 (2014).
- [57] S. Naghavi, S. Chadov, C. Felser, G. H. Fecher, J. Kübler, K. Doll, and M. Jansen, Pressure induced insulator/half-metal/metal transition in a strongly correlated p -electron system, *Phys. Rev. B* **85**, 205125 (2012).
- [58] J. Winterlik, G. H. Fecher, C. A. Jenkins, S. Medvedev, C. Felser, J. Kübler, C. Mühle, K. Doll, M. Jansen, T. Palasyuk, I. Trojan, M. I. Eremets, and F. Emmerling, Exotic magnetism in the alkali sesquioxides Rb_4O_6 and Cs_4O_6 , *Phys. Rev. B* **79**, 214410 (2009).
- [59] A. K. Nandy, P. Mahadevan, P. Sen, and D. D. Sarma, KO_2 : Realization of orbital ordering in a p -orbital system, *Phys. Rev. Lett.* **105**, 056403 (2010).
- [60] A. K. Nandy, P. Mahadevan, and D. D. Sarma, K_2O_2 : The most stable oxide of K, *Phys. Rev. B* **84**, 035116 (2011).
- [61] W. Cai, J. He, H. Li, R. Zhang, D. Zhang, D. Y. Chung, T. Bhowmick, C. Wolverton, M. G. Kanatzidis, and S. Deemyad, Pressure-induced ferroelectric-like transition creates a polar metal in defect antiperovskites $\text{Hg}_3\text{Te}_2\text{X}_2$ ($X = \text{Cl}, \text{Br}$), *Nat. Commun.* **12**, 1509 (2021).
- [62] T. Saha-Dasgupta, Double perovskites with 3d and 4d/5d transition metals: Compounds with promises, *Mater. Res. Express* **7**, 014003 (2020).
- [63] L. M. Sandratskii, Exchange interactions in $(\text{ZnMn})\text{Se}$: LDA and LDA+U calculations, *Phys. Rev. B* **68**, 224432 (2003).
- [64] M. Sahakyan and V. H. Tran, The density functional theory study of substitution effect in antiferromagnetic $\text{USn}_{0.5}\text{Sb}_{1.5}$, *J. Solid State Chem.* **312**, 123174 (2022).
- [65] F. Birch, Finite strain isotherm and velocities for single-crystal and polycrystalline NaCl at high pressures and 300 °K, *J. Geophys. Res.* **83**, 1257 (1978).
- [66] M. Beekman, A. J. Karttunen, W. Wong-Ng, M. Zhang, Y.-S. Chen, C. Posadas, A. Jarymowycz, E. Cruse, W. Peng, A. Zevalkink, J. A. Kaduk, and G. S. Nolas, Thermal and mechanical properties of the clathrate-II $\text{Na}_{24}\text{Si}_{136}$, *Phys. Rev. B* **105**, 214114 (2022).
- [67] S. Zhang, R. Paul, S. X. Hu, and M. A. Morales, Toward an accurate equation of state and B1-B2 phase boundary for magnesium oxide up to terapascal pressures and electron-volt temperatures, *Phys. Rev. B* **107**, 224109 (2023).